Intense relativistic electron beam propagation in evacuated drift tubes

P. G. O'Shea, D. Welsh, W. W. Destler, and C. D. Striffler
Laboratory for Plasma and Fusion Energy Studies and the Electrical Engineering Department, University of Maryland, College Park, Maryland 20742

(Received 8 November 1983; accepted for publication 19 January 1984)

The propagation of a magnetically confined intense relativistic electron beam (IREB) (1 MeV, 27 kA, 20 ns FWHM) in vacuum drift tubes has been studied experimentally and theoretically. Experimental results for current propagation as a function of uniform applied magnetic field (0–1.2 T) are presented for various drift tube diameters, cathode geometries, and anode aperture sizes. An analytic model of laminar beam flow is presented which predicts the space-charge-limited current of a solid IREB propagating in a grounded drift tube. A steady-state equilibrium is examined and is compared with the experimental results.

PACS numbers: 41.80.Dd, 52.40.Mj, 52.60. + h, 41.70. + t

I. INTRODUCTION

In recent years, the generation and propagation of intense relativistic electron beams (IREB) have been the subjects of many theoretical and experimental studies, in part due to the various applications of such beams in such diverse fields as high power coherent radiation source development,[1–3] collective ion acceleration,[4–7] and plasma heating and confinement.[8,9] A summary of the field prior to 1982 is presented in the book by R. B. Miller.[10]

With respect to beam propagation, one distinguishes between (a) propagation in vacuum, (b) propagation in a plasma, and (c) propagation in a neutral gas. Each of these areas can be divided into operating regimes which depend on the focusing field in (a), on plasma density and temperature in (b), and on the gas pressure in (c). Furthermore, beam propagation can be described in terms of fundamental limits such as the space-charge-limiting current I_L in (a), the Alfvén–Lawson current I_A in (b) and (c), or other limiting effects such as instabilities. Thus, in a vacuum drift tube and in the absence of charge neutralizing positive ions, an IREB with a current $I \leqslant I_L$ can propagate and then over significant distances only if a focusing magnetic field is present. A distinction is made between systems in which the cathode is either immersed or not immersed in the confining magnetic field.[11] In the former case, one finds that in the regime of high magnetic field ($B \rightarrow \infty$) the electrons are forced to move along field lines. The space-charge-limiting current in this extreme is the well-known formula for I_L by Bogdankevich and Rukhadze,

$$I_L = I_0 \frac{(\gamma_0^{2/3} - 1)^{3/2}}{1 + 2 \ln \dfrac{R_w}{R_b}}, \tag{1}$$

where $I_0 = 4\pi\epsilon_0 mc^3/q = 1.7 \times 10^4$ A for electrons, R_b = beam radius, R_w = radius of the drift tube, and $(\gamma_0 - 1)mc^2 = eV_0$ = kinetic energy of the electron at the plane of injection into the drift tube. In actual laboratory experiments where the magnetic field is typically constrained to values in the range 0–2 T, this result must be modified to include internal electron beam dynamics in such systems.

Both analytical theories and numerical simulations of such systems have been reported,[12–17] but to date a systematic experimental study of these phenomena has not been available for comparison with theory and simulation. In this paper, we describe the results of an experimental study of intense electron beam propagation in evacuated drift tubes of various diameters in the presence of a nearly uniform applied magnetic field. These results, presented in Sec. II, are then compared to results expected from an analytical model presented in Sec. III. Conclusions are drawn in Sec. IV.

II. EXPERIMENTS

The general experimental configuration is shown in Fig. 1. An intense relativistic electron beam (1 MeV, 27 kA, 30 ns FWHM) was field emitted from a 1-cm-diam stainless steel cathode situated 1.2 cm upstream of a stainless steel anode plate. Two different cathode geometries were used as shown in Fig. 2, and will be referred to as "solid" and "hollow" cathodes, respectively. Anode apertures of 1.2 and 2.6 cm were used in combination with stainless steel drift tubes

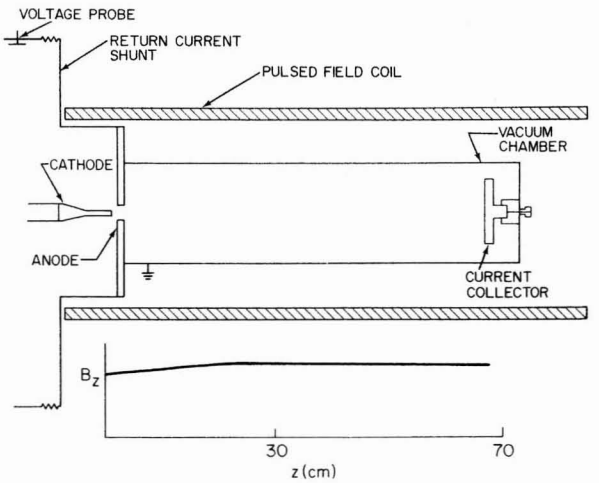

FIG. 1. Experimental configuration and applied axial magnetic field profile.

 0021-8979/84/113934-06$02.40

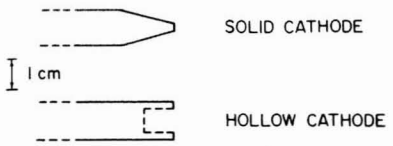

FIG. 2. "Solid" and "hollow" cathode geometries.

of 3.8, 9.8, and 14.8 cm i.d. An axial magnetic guide field in the range 0–1.2 T constrained the radial motion of the beam electrons over the entire experimental length from cathode to current collector. The beam current propagating to the end of the drift tube was measured using a low impedance current collector. In the collector, electron current was absorbed in a graphite beamstop and flowed to ground through a 14-mΩ stainless steel foil shunt. The injected beam current was measured by placing the collector 2 cm downstream of the anode plane and was found to be consistently 27 ± 1 kA with no appreciable variation with applied magnetic field. The vacuum maintained both upstream and downstream of the anode was in the range 10^{-5}–10^{-4} Torr.

The peak electron beam current I measured at the downstream end of the 70-cm-long drift tube as a function of applied magnetic field B is shown in Figs. 3 and 4 for the various geometries considered. Characteristic oscilloscope traces, giving beam current as a function of time, are shown in Fig. 5.

The following important features are apparent from our measurements.

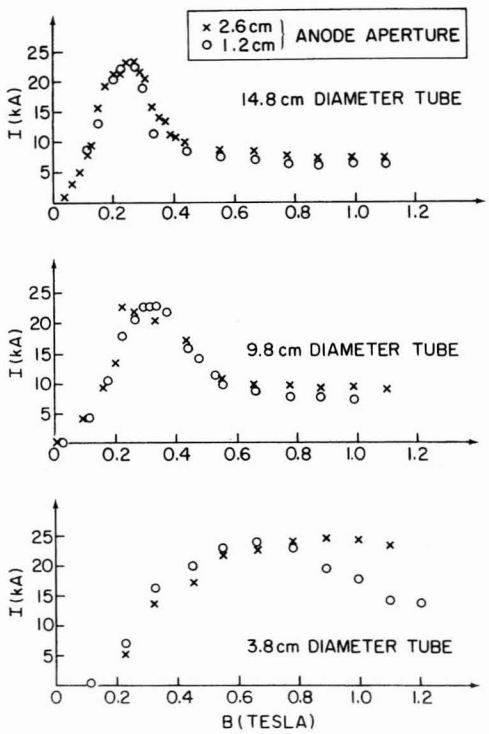

FIG. 3. Peak propagating current measured at current collector for 14.8-, 9.8-, 3.8-cm-diam drift tubes, and 2.6- and 1.2-cm-diam anode apertures using *solid cathode*.

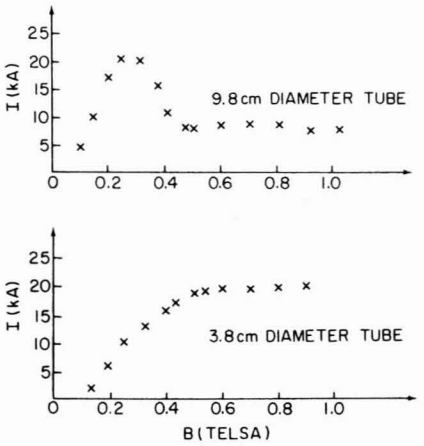

FIG. 4. Peak propagating current measured at current collector for 9.8- and 3.8-cm-diam drift tubes with 2.6-cm-diam anode aperture and *hollow cathode*.

(1) Without applied magnetic field, less than 0.5 kA of beam current was observed to propagate to the end of any of the drift tubes.

(2) In all tubes there appear to be three distinct regimes of beam propagation. However, these distinctions are more obvious in the 14.8- and 9.8-cm-diam tube results.

(a) *Low magnetic field.* Propagating current initially rises as B is increased from zero. Here we have a poorly confined beam, a significant fraction of which may hit the tube wall and be lost. As B increases, the beam confinement improves and more current propagates.

(b) *Intermediate magnetic field.* Beam current decreases rapidly with increasing B, and space-charge effects due to the relationship between beam and tube radius are playing an increasingly significant role in this region.

(c) *High magnetic field.* A plateau region where the change in propagating current is small as B increases.

(3) As tube diameter decreases, the region of maximum current propagation shifts to higher magnetic fields and also the propagating current in the high field plateau region increases.

(4) For the 14.8- and 9.8-cm-diam tubes, changing the anode aperture size from 1.2 to 2.6 cm diam did not greatly

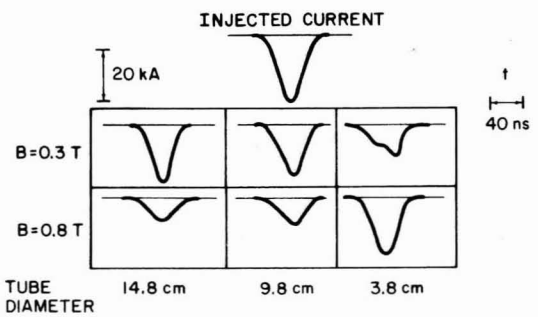

FIG. 5. Oscilloscope tracings of typical current collector pulse shapes, indicating injected current waveform and downstream current waveform, for applied magnetic fields of 0.3 and 0.8 T in 14.8-, 9.8- and 3.8-cm-diam drift tubes using 2.6-cm-diam aperture and solid cathode.

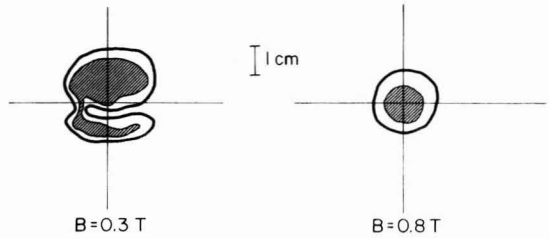

FIG. 6. Tracings of witness plate damage patterns for applied magnetic fields of 0.3 and 0.8 T in 3.8-cm-diam tube using 2.6-cm-diam anode aperture and solid cathode. Shaded areas indicate region of most intense damage. Outer boundary indicates extent of observable damage.

alter the propagating current except in the high field plateau region. However, we note significant difference in the current characteristics for the high field region between the 1.2- and 2.6-cm anode hole cases for the 3.8-cm tube. This is due to the fact that the anode diameter is a significant fraction of the tube diameter. The smaller anode hole case appears to exhibit similar features in the region $0.8 \lesssim B \lesssim 1.1$ T as the large tubes do in the range $0.3 \lesssim B \lesssim 0.5$ T. We have evidence that the current propagating in this tube for the 2.6 anode begins to decrease at $B = 1.2$ T and above, but limitations on our pulsed magnetic field coils prevent us from operating reproducibly in this region.

(5) The hollow cathode data differs from the solid cathode data primarily by a small difference in the magnitude of the propagated currents as a given magnetic field.

The fact that the smallest tube can propagate as much current at high B as the large ones can at considerably lower B removes from consideration the possibility that some form of magnetic mirroring, resulting from nonuniformity of the applied field causes the observed reduction of current in the large tubes at high magnetic field.

A further series of experiments was carried out using the solid cathode and 9.8-cm drift tube in which the 2.6-cm anode hole was covered at the cathode side by a 25-μ-thick titanium foil. In these tests, no significant deviations from the current propagation characteristic of the foilless diode case were observed.

Experiments were also performed to measure the beam cross section at the downstream end of the 9.8-cm drift tube using Mylar witness plates. Two characteristic witness plate patterns are exhibited in Fig. 6. For $B \gtrsim 0.4$ T, the pattern is circular and well defined, the diameter being approximately constant 2.3 cm. However, for $0.2 \leqslant B \leqslant 0.4$ T, the pattern indicated a filamentary beam such as the bifurcated pattern shown for 0.3 T. Tests with axially stacked plates indicate that this filamentary pattern was rotating about the axis of propagation. Such patterns appear to be characteristic of an $m = 2$ or higher-order type instability of the beam in the high current propagation region.

III. MODEL OF SOLID BEAM EQUILIBRIUM

A steady-state model of an intense relativistic electron beam in an axis-symmetric system can be constructed by conserving single particle energy, conserving canonical angular momentum, applying continuity of current, and maintaining force balance on each element of the beam. The parameters we consider are shown in Fig. 7, and they represent the experimental system discussed in Sec. II. Specifically, we assume that a solid, uniform density electron beam of radius R_a is injected into a long grounded cylindrical drift tube of radius R_w. The injected beam is irrotational and monoenergetic with energy $mc^2(\gamma_0 - 1) = eV_0$. After the beam passes through the anode end of the drift tube, we assume it expands adiabatically to a radius R_b where a laminar flow equilibrium is set up far from the end walls. The entire system is immersed in a uniform axial magnetic field B_{AZ}. The downstream beam properties are the charge density $\rho(r)$, and the azimuthal and axial velocities, $V_\phi(r)$ and $V_z(r)$. We assume the fields generated by the beam are confined inside the drift tube. These self-fields, which are shown in Fig. 7, include the radial electric field $E_{sr}(r)$ as well as the azimuthal and axial magnetic fields, $B_{s\phi}$ and B_{sz}.

To further simplify the analysis, we assume the equilibrium beam density is constant across the beam cross section, $\rho(r) = \rho_b$. Because of this assumption, the electric potential $\phi(r)$ and the electric field $E_{sr}(r) = -\partial\phi(r)/\partial r$ are easily calculated. Now by conserving single particle energy, we can write the kinetic energy of the beam, $\mathrm{KE} = mc^2[\gamma(r) - 1]$ in terms of the electric potential,

$$\gamma(r) = \gamma_0 + \frac{e}{mc^2}\phi(r) = \frac{1}{\sqrt{1 - \beta_\phi^2(r) - \beta_z^2(r)}}, \tag{2}$$

where

$$\phi(r) = \frac{\rho_b R_b^2}{4\epsilon_0}\left(1 - \frac{r^2}{R_b^2} + 2\ln\frac{R_w}{R_b}\right), \tag{3}$$

$\beta_\phi(r) = V_\phi(r)/c$ and $\beta_z(r) = V_z(r)/c$.

In a laminar flow beam of uniform density, the relative radial position of an electron in the beam is constant regardless of beam radius, i.e., $r_a/R_a = r/R_b$ where r_a is the radial position of the particle as it passes through the anode plane and r is the radial position of the particle downstream. For this case, canonical angular momentum is conserved totally in terms of the downstream beam radius. We obtain

$$-\frac{eB_{AZ}r_a^2}{2} = -\frac{eB_{AZ}r^2}{2}\left(\frac{R_a}{R_b}\right)^2 = r[m\gamma(r)V_\phi(r) - eA_\phi(r)], \tag{4}$$

where $A_\phi(r)$ is the downstream total azimuthal component of the magnetic vector potential. Solving Eq. (4) for $V_\phi(r)$ and substituting it into $J_\phi(r) = \rho_b V_\phi(r)$, noting that $A_\phi(r)$

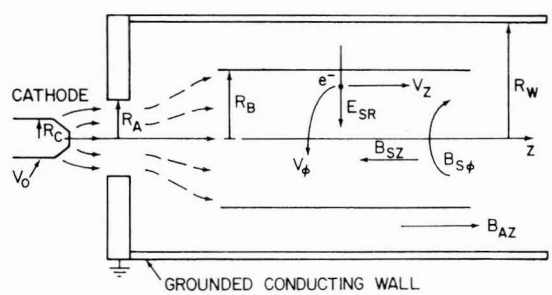

FIG. 7. Schematic of beam model.

$= rB_{AZ}/2 + A_{s\phi}(r)$, we obtain from Maxwell's Equations, $\nabla \times \mathbf{B}_s = -\nabla^2 \mathbf{A}_s = \mu_0 \mathbf{J}_s$,

$$\frac{\partial}{\partial r}\frac{1}{r}\frac{\partial}{\partial r} rA_{s\phi}(r) + \frac{e}{m}\frac{\mu_0 \rho_b}{\gamma(r)} A_{s\phi}(r) = -\frac{1}{2}\frac{e}{m}\frac{\mu_0 \rho_b}{\gamma(r)} B_{AZ}\left(1 - \frac{R_a^2}{R_b^2}\right) r, \quad 0 < r < R_b , \tag{5a}$$

$$\frac{\partial}{\partial r}\frac{1}{r}\frac{\partial}{\partial r} rA_{s\phi}(r) = 0 , \quad R_b < r < R_w . \tag{5b}$$

After expanding $\gamma(r)$ in terms of ρ_b from Eq. (2), Eq. (5) can be solved by Frobenius' Method. The boundary conditions are: $A_{s\phi}(r=0) = 0$, $A_{s\phi}$ and B_{sz} are continuous across the beam edge $r = R_b$, and $A_{s\phi}(r = R_w) = 0$. The general solution inside the beam is

$$A_{s\phi}(r) = \frac{B_{AZ}\left(1 - \frac{R_a^2}{R_b^2}\right) r}{2(1+\xi)} \times \left[-\xi + \sum_{n=1}^{\infty} \prod_{i=1}^{n} \frac{i(i-1)-1}{i(i+1)} K^n \left(\frac{r}{R_b}\right)^{2n} \right], \tag{6}$$

where

$$K = \frac{\frac{1}{4}\frac{e}{m}\mu_0 \rho_b R_b^2}{\gamma_0 + \frac{1}{4}\frac{e}{m}\mu_0 \rho_b R_b^2 \left(1 + 2\ln\frac{R_w}{R_b}\right)}$$

and

$$\xi = \sum_{n=1}^{\infty} \prod_{i=1}^{n} \frac{i(i-1)-1}{i(i+1)} K^n \left[n\left(1 - \frac{R_b^2}{R_w^2}\right) + 1 \right].$$

Now $B_{sz}(r)$ is computed from $\mathbf{B}_s = \nabla \times \mathbf{A}_s$ and $V_\phi(r)$ is calculated from Eq. (4). Then, $V_\phi(r)$ and Eq. (2) are used to find $V_z(r)$. Finally, the azimuthal self-magnetic field $B_{s\phi}(r)$ can be calculated from $V_z(r)$ and Ampere's Law.

At this point, the functional forms of all the equilibrium beam properties have been found in terms of R_a, R_b, R_w, γ_0, B_{AZ}, and the beam density ρ_b. These quantities can be determined by requiring each volume element of the beam to be in radial force balance. Radial force balance can be written

$$\frac{m\gamma(r)V_\phi^2(r)}{r} = e\{E_{sr}(r) + V_\phi(r)[B_{AZ} + B_{sz}(r)] - V_z(r)B_{s\phi}(r)\} \tag{7}$$

for our model. To solve this equation, R_a, R_b, R_w, γ_0, and B_{AZ} are held fixed while ρ_b is varied until the "best possible equilibrium" is found. Because of our uniform density assumption, there is no total radial force balance, but Fig. 8 shows a typical "best possible equilibrium" and the net force balance is good. All of our "equilibria" had three features in common with Fig. 8: (a) there is exact force balance between $r/R_b = 0.5$ and $r/R_b = 0.6$, (b) the net radial force is smaller than any of the individual forces, and (c) the force imbalance shows a stable configuration with outward forces in the beam's core and inward forces on the beam's edge. The velocity profiles for this beam are included for completeness. After calculating the beam density for an equilibrium, the axial beam current is calculated from

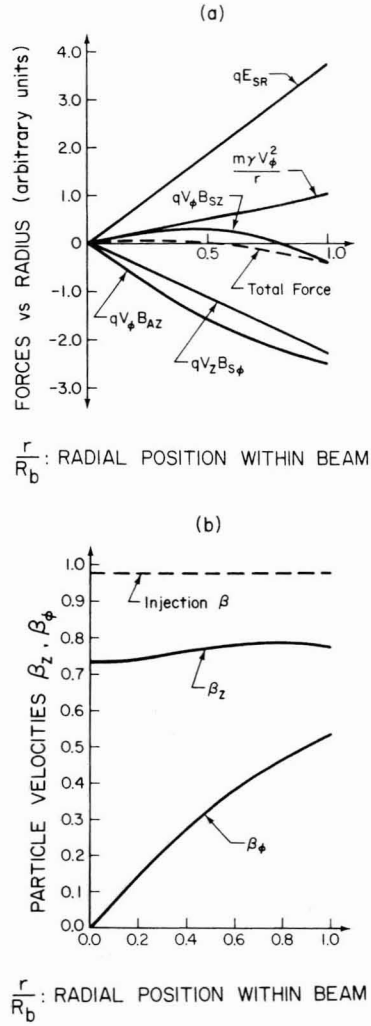

FIG. 8. Equilibrium force and velocity profiles for typical downstream beam. The parameters are : $R_a = 1.3$ cm, $R_w = 4.8$ cm, $\gamma_0 = 3.5$, $B_{AZ} = 0.16$ T, $R_b = 4.0$ cm, and $I = 19.4$ kA. Point D of Figs. 9 and 10.

$$I = 2\pi\rho_b \int_0^{R_b} V_z(r)\, r dr , \tag{8}$$

where we have assumed this current equals the injected current.

A set of results displaying the interdependencies of all the variables is shown in Fig. 9. The fixed parameters are $R_a = 1.3$ cm, $R_w = 4.8$ cm, and $\gamma_0 = 3.5$ (a 1.28-MeV beam). We have plotted normalized electrostatic potential on the beam axis, $\phi(r=0)/eV_0$, versus beam current I in kA. The solid lines represent constant beam radii R_b and the dashed lines represent constant applied magnetic field B_{AZ}. One can read this graph as follows; choose an applied magnetic field B_{AZ} and an injected current, then follow the magnetic field line until the current is reached. If this is not possible, the maximum current propagated is less than the injected current for this B_{AZ}. Otherwise, the beam has expanded to a radius R_b and has attained radial force balance.

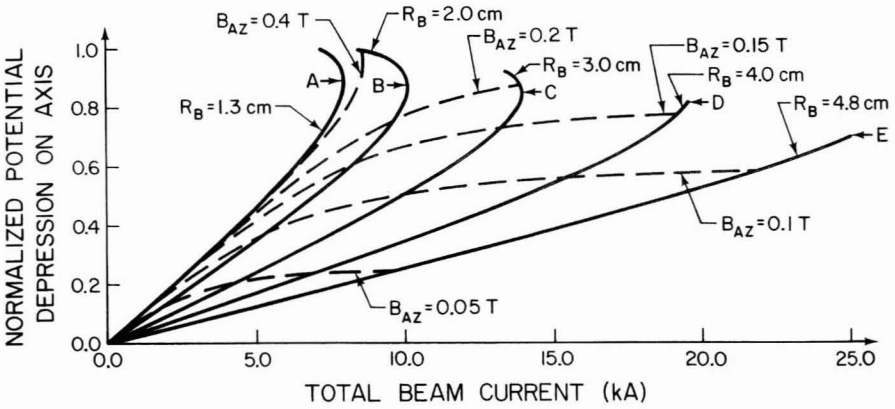

FIG. 9. Downstream beam properties for $R_a = 1.3$ cm, $R_w = 4.8$ cm, and $\gamma_0 = 3.5$. Normalized potential depression on axis vs axial current with beam radius R_b and applied magnetic field B_{AZ} as parameters.

As an example, if $B_{AZ} = 1.0$ kG and 10 kA is injected, the beam expands to $R_b = 3.0$ cm and the potential depression on the beam axis is 0.5 of the diode potential. Notice that no more than 22 kA will propagate at 1.0 kG.

To compare the theoretical predictions to the experimental results, we generated Fig. 10 from the data in Fig. 9. This is done by starting at the infinite magnetic field limit where $R_b = R_a$. The maximum current propagated for this situation is about 8 kA and is indicated by Point A in Fig. 9. Point A and the Bogdankevich–Rukhadze limiting current of Eq. (1) are both displayed in Fig. 10 ($I_{BR} = I_L$). Now, as the magnetic field is lowered, the beam will expand to some new $R_b > R_a$. When $R_b = 2.0$ cm, the necessary applied field for maximum current propagation is approximately 2.5 kG, and $I_{max} = 10$ kA (Point B). Following this argument generates the I_{max} vs B_{AZ} curve from Point A through Point B to Point C. In this region, the beam current is space charge limited. This means the electrostatic potential energy of the beam near the axis is large enough to regulate the current flow. For example, if the beam density were increased at Point B, less current would flow because the center of the beam has so little kinetic energy.

As the magnetic field is decreased from its value at Point C, the beam continues to expand, and the limiting current moves from Point C through Point D to Point E in Fig. 9. For magnetic field strengths in this regime, the lines of constant beam radius end prematurely at Points D and E because the current is limited by the total field energy of the beam. If the current density increases for the beam at Point D or E, the field energy generated by the beam becomes larger than the kinetic energy of the beam and steady state cannot be achieved.

Finally, for magnetic fields lower than at Point E, the beam fills the drift tube $R_b = R_w$ and current is limited by the size of the tube. In Fig. 11, we have generated the I_{max} vs B_{AZ} curve for a wall radius $R_w = 1.905$ cm, $\gamma_0 = 3.5$, and two different anode radii, $R_a = 1.27$ and 0.635 cm. For these cases, I_{BR} is shown for reference.

In comparing Figs. 3, 10, and 11, it is clear that the theory predicts all the trends discussed in Sec. II. The only disagreement is the magnitude of the applied magnetic field. Here, the theory is off by approximately a factor of 2. It is expected that cyclotron motions, other nonlaminar effects, and nonadiabatic expansions will account for some of this discrepancy.

IV. SUMMARY AND DISCUSSION

We have performed experiments to determine the maximum current that can propagate down a cylindrical drift tube. The current source is nominally a 1-MV, 30-kA, 30-ns electron beam which enters one end (that serves as the anode) of a long cylindrical tube ($L \gg R$). The maximum propagated

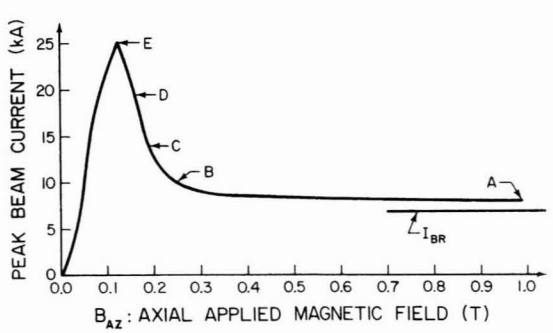

FIG. 10. Maximum beam current vs applied magnetic field for $R_a = 1.3$ cm, $R_w = 4.8$ cm, and $\gamma_0 = 3.5$. The same case as Fig. 9.

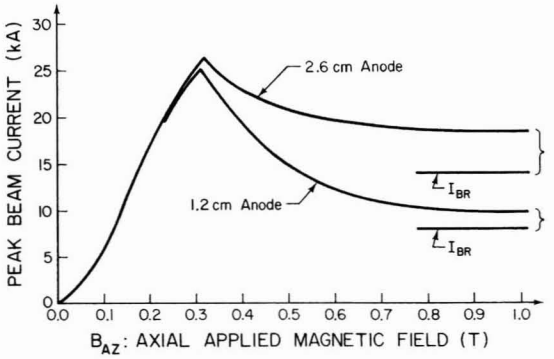

FIG. 11. Maximum beam current vs applied magnetic field for $R_w = 1.9$ cm and $\gamma_0 = 3.5$. Two different anode sizes are shown: $R_a = 0.6$ cm and $R_a = 1.3$ cm.

current is examined as a function of tube radius, anode hole size, and applied magnetic field. For solid cathodes these results are displayed in Fig. 3 and for a hollow cathode in Fig. 4.

In an attempt to understand these results, a steady-state, azimuthally symmetric beam model is presented and self-consistently solved to determine the downstream beam properties for an injected solid, monoenergetic, uniform current density electron beam. Further restrictions of the model are laminar flow and uniform charge density after it has reached an axial position. These results, in the same form as the experimental results, are shown in Figs. 10 and 11. Detailed comparisons should only be made between the solid cathode data of Fig. 3 and the analytical results of Figs. 10 and 11.

The model and experiments agree with respect to general shape of the maximum current as a function of applied magnetic field. This is true for all variations in the ratio of tube radius to anode hole size. The three regimes of magnetic field operation are: low field regime, where the beam is poorly confined and a significant fraction is lost to the tube walls; intermediate field regime, where the beam current is confined within the tube walls but space-charge potential depression causes a decrease in net current propagated; and high field regime, where the net current propagated remains relatively constant with further increase in the field. The model and experiment agree with the uncertainty of the diode voltage as to the quantitative peak value of the current as well as the propagated current in the high magnetic field regime. The main disagreement between the model and experiments is the value of the magnetic field at which the peak current propagates. This value is a factor of 2 larger in the experiments than in the model.

We would like to comment on a few effects which we believe could be important and would help to explain some of our differences. The full injected current of 30 kA is never seen to propagate the length of the system. Thus, in almost all experiments a virtual cathode is formed near the entrance end of the drift tube. Clearly the analytic model does not include this condition or the effects resulting from it. The actual radial extent of the virtual cahtode is probably a strong function of magnetic field and a more appropriate model should think of the virtual cathode as the entering surface versus the anode plane. A related issue is the laminar flow assumption in our model. Initial analytic studies involving cyclotron orbit effects indicate a shift of the $I_{\max}$ vs B_{AZ} curve to higher values of B_{AZ}.

In summary, the comparisons between an experiment and a fairly simple model that concentrates on determining the maximum current that can propagate in an evacuated drift tube as a function of applied magnetic has produced fairly good agreement and understanding of this system.

ACKNOWLEDGMENTS

We wish to acknowledge helpful discussions with M. Reiser. Excellent technical assistance was provided by J. Pyle. This work was supported by the Air Force Office of Scientific Research, the U.S. Department of Energy, and the University of Maryland Computer Science Center.

[1]J. L. Herschfield and V. L. Granatstein, IEEE Trans. Microwave Theory Tech. **MTT-25**, 522 (1977).
[2]E. Ott and R. V. Lovelace, Appl. Phys. Lett. **27**, 378 (1975).
[3]G. Bekefi and T. J. Orzechowski, Phys. Rev. Lett. **37**, 379 (1976).
[4]C. L. Olson and U. Schumacker, in *Springer Tracts in Modern Pysics: Collective Ion Acceleration*, edited by G. Hobler (Springer, New York, 1979).
[5]S. Graybill and J. Uglum, J. Appl. Phys. **41**, 236 (1970).
[6]W. W. Destler, L. E. Floyd, and M. Reiser, Phys. Rev. Lett. **44**, 70 (1980).
[7]R. Adler, J. A. Nation, and V. Serlin, Phys. Fluids **24**, 347 (1981).
[8]C. A. Kapetanakos and W. M. Black, Bull. Am. Phys. Soc. **18**, 1264 (1973).
[9]M. Friedman, Phys. Rev. Lett. **24**, 1098 (1970).
[10]R. B. Miller, *An Introduction to the Physics of Intense Charged Particle Beams* (Plenum, New York, 1982).
[11]M. Reiser, Phys. Fluids **20**, 477 (1977).
[12]L. S. Bogdankevich and A. A. Rukhadze, Usp. Fiz. Nauk. **103**, 609 (1971) [Sov. Phys. Usp. **14**, 163 (1971)].
[13]J. R. Thompson and M. L. Sloan, Phys. Fluids **21**, 2032 (1978).
[14]L. E. Thode, B. B. Godfrey, and W. R. Shanahan, Phys. Fluids **22**, 747 (1979).
[15]P. G. O'Shea, W. W. Destler, C. D. Striffler, and D. Welsh, Bull. Am. Phys. Soc. **27**, 983 (1983).
[16]W. W. Destler, P. G. O'Shea, M. Reiser, C. D. Striffler, D. Welsh, and H. H. Fleishmann, IEEE Trans. Nucl. Sci. **NS-30**, 3183 (1983).
[17]D. Welsh, C. D. Striffler, P. G. O'Shea, and W. W. Destler, Bull. Am. Phys. Soc. **28**, 1039 (1983).